Electrochemical Testing and Benchmarking of Compositionally Complex Lithium Argyrodite Electrolytes for All-Solid-State Battery Application

Jianxuan Du+,[a] Jing Lin+,[a] Ruizhuo Zhang,[a] Shuo Wang,[b, c] Sylvio Indris,[d] Helmut Ehrenberg,[d] Aleksandr Kondrakov,[a, e] Torsten Brezesinski,*[a] and Florian Strauss*[a]

Ceramic ion conductors play a pivotal role as electrolytes in solid-state batteries (SSBs). Aside from the ionic conductivity, their (electro)chemical stability has a profound effect on the performance. Lithium thiophosphates represent a widely used class of superionic materials, yet they suffer from limited stability and are known to undergo interfacial degradation upon battery cycling. Knowledge of composition-dependent properties is essential to improving upon the stability of thiophosphate solid electrolytes (SEs). In recent years, compositionally complex (multicomponent) and high-entropy lithium

argyrodite SEs have been reported, having room-temperature ionic conductivities of $\sigma_{ion} > 10$ mS cm^{-1}. In this work, various multi-cationic and -anionic substituted argyrodite SEs are electrochemically tested via cyclic voltammetry and impedance spectroscopy, as well as under operating conditions in SSB cells with layered Ni-rich oxide cathode and indium-lithium anode. Cation substitution is found to negatively affect the electrochemical stability, while anion substitution (introducing Cl$^-$/Br$^-$ and increasing halide content) has a beneficial effect on the cyclability, especially at high current rates.

1. Introduction

Bulk-type solid-state batteries (SSBs) are emerging as a promising next-generation electrochemical energy-storage technology. The implementation of inorganic solid electrolytes (SEs) instead of organic liquid electrolytes may possibly help to increase the energy and power density of battery cells and to improve safety.[1,2] For realizing this, highly conducting and (electro)chemically stable SEs are needed, which ideally should

also be mechanically flexible to accommodate for volume changes of the active electrode materials during cycling.[3–6]

In search of suitable materials, lithium argyrodites (Li$_6$PS$_5$X, with X=Cl, Br, I) have been recognized as one of the most promising classes of SEs. This is due in part to high room-temperature ionic conductivities of $\sigma_{ion} > 1$ mS cm^{-1},[7–10] along with favorable mechanical properties, the latter allowing to effectively establish intimate contact with the active electrode materials and for facile cell assembly (without the need for sintering).[11,12] Moreover, the ion mobility in lithium argyrodites can be altered by iso- or aliovalent substitution on the phosphorus, sulfur, and halide sites or by increasing the halide content, referring to halogen-rich SEs with the general formula Li$_{5.5}$PS$_{4.5}$X$_{1.5}$ (X=Cl, Br).[13–18] This has led to the discovery of materials, either cationic or anionic substituted, showing ionic conductivities exceeding 10 mS cm^{-1} at room temperature.[13,14,17,19] However, literature is lacking thorough electrochemical evaluation of highly conducting lithium argyrodites, making rational optimization difficult. This not only pertains to conductivity, but also to stability.

Recently, we have reported on high-entropy lithium argyrodites as a novel class of chemically complex SEs with high ionic conductivities, even in a cold-pressed state.[16,18,20] Despite varying anion and cation compositions, several of these materials exhibit room-temperature ionic conductivities of $\sigma_{ion} \geq 10$ mS cm^{-1}. This now allows to test different SEs of similar ionic conductivity in SSB cells using a layered Ni-rich oxide cathode active material, namely LiNi$_{0.85}$Co$_{0.10}$Mn$_{0.05}$O$_2$ (NCM851005). Specifically, employing Li$_{6.5}$[P$_{0.25}$Si$_{0.25}$Ge$_{0.25}$Sb$_{0.25}$]S$_5$I (equimolar), Li$_{6.67}$[P$_{0.16}$Si$_{0.5}$Ge$_{0.16}$Sb$_{0.16}$]S$_5$I (Si-rich), Li$_{6.67}$[P$_{0.16}$Si$_{0.16}$Ge$_{0.5}$Sb$_{0.16}$]S$_5$I (Ge-rich), Li$_{5.5}$PS$_{4.5}$Cl$_{0.8}$Br$_{0.7}$ (I-free), and Li$_6$PS$_5$Cl (LPSCl), we examine the effect that the composition of the superionic SE has on the electrochemical stability and

[a] *J. Du,+ J. Lin,+ R. Zhang, Dr. A. Kondrakov, Dr. T. Brezesinski, Dr. F. Strauss*
Battery and Electrochemistry Laboratory (BELLA), Institute of Nanotechnology, Karlsruhe Institute of Technology (KIT), Kaiserstr. 12, 76131 Karlsruhe, Germany
E-mail: torsten.brezesinski@kit.edu
florian.strauss@kit.edu

[b] *Prof. S. Wang*
Center of Smart Materials and Devices, State Key Laboratory of Advanced Technology for Materials Synthesis and Processing, School of Material Science and Engineering, Wuhan University of Technology, Wuhan 430070, China

[c] *Prof. S. Wang*
Foshan (Southern China) Institute for New Materials, Foshan 528200, China

[d] *Dr. S. Indris, Prof. H. Ehrenberg*
Institute for Applied Materials-Energy Storage Systems (IAM-ESS), Karlsruhe Institute of Technology (KIT), Kaiserstr. 12, 76131 Karlsruhe, Germany

[e] *Dr. A. Kondrakov*
BASF SE, Carl-Bosch-Str. 38, 67056 Ludwigshafen, Germany

[+] *Contributed equally to this work.*

battery performance. Using cyclic voltammetry (CV), time-resolved electrochemical impedance spectroscopy (EIS), and galvanostatic charge-discharge tests, we demonstrate that anion prevails over cation substitution.

2. Results and Discussion

Initially, X-ray diffraction (XRD) measurements were performed to determine the crystal structure and confirm phase purity of the synthesized SEs. Figure 1 shows the respective XRD patterns, along with that collected from the commercially available LPSCl, which served as a benchmark SE, indicating that the materials are single-phase argyrodites. Aside from the presence of Li_2S and/or LiI trace impurities (unreacted precursors), the reflections can be indexed to the F-43m space group.[7] For the cationic substituted samples, Rietveld refinement of the diffraction data was carried out (see Tables S1–S3, Supporting Information), while Le Bail analysis was performed for the anionic substituted (I-free) material both to determine the lattice parameter and quantify the fraction of crystalline impurities (see Figure S1a–d, Supporting Information). As evident from Table 1, the equimolar, Ge-rich, and Si-rich SEs exhibit a larger lattice parameter than the I-free sample due to the larger ionic radius of iodine compared to chlorine and bromine.[21] Also, the differences observed in the lattice parameter for the equimolar, Ge-rich, and Si-rich SEs align with variations in ionic radii considering the different stoichiometry of the materials. The ionic conductivities determined on cold-pressed pellets at room temperature are given in Table 1. They varied from $\sigma_{ion} \approx 3$ mS cm^{-1} for LPSCl to around 15 mS cm^{-1} for the Ge-rich SE.

The electrochemical stability of the as-prepared materials was investigated by CV measurements conducted on cells with SE/carbon black composite as working electrode, SE as separator layer, and indium-lithium alloy as counter electrode. This configuration allows to assess the electrochemical stability window (ESW) of the different SEs.[22,23] Figure 2a shows the first-cycle CV curves at 0.1 mV s^{-1} and at 45 °C, with the current normalized to the mass of SE in the working electrode. Asymmetric current peaks were observed for all SEs, indicating that (electrochemically driven) side reactions occur, independent of the composition. The potential range of the initial sweep was from open-circuit voltage (OCV) to 3.68 V vs. In/InLi (~4.3 V vs. Li$^+$/Li). For the cationic substituted SEs, a steep increase in
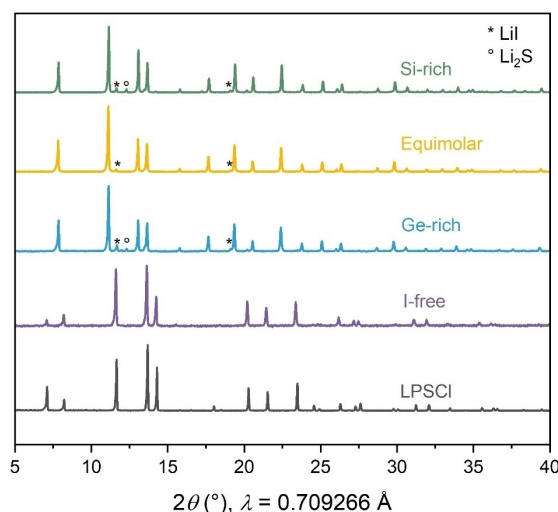

Figure 1. XRD patterns collected from the different SEs. Trace impurities of unreacted precursors are denoted by symbols.

specific current was noticed around 2.0 V (~2.62 V vs. Li$^+$/Li). In contrast, for LPSCl and the I-free SE, the current onset was detected at about 2.22 and 2.27 V (~2.84 and 2.89 V vs. Li$^+$/Li), respectively. In general, this can be attributed to sulfide oxidation to polysulfides of different chain lengths [i.e., $nS^{2-} \rightarrow S_n^{2-} + (2n-2)e^-$]. The lower onset potential found for the cationic substituted samples implies a lower anodic stability compared to both the anionic substituted SE and LPSCl. It has been reported that the oxidative decomposition of LPSCl results in the formation of LiCl, P_2S_5, and S (or S_8) according to Equation 1.[24,25]

$$Li_6PS_5Cl \rightarrow LiCl + \frac{1}{2}P_2S_5 + \frac{5}{2}S + 5Li^+ + 5e^- \qquad (1)$$
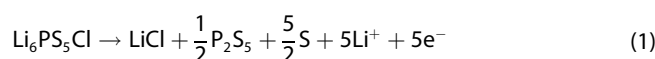
However, this equation is simplified as the underlying reaction steps are most likely mechanistically more diverse, possibly involving the formation of a variety of thiophosphates, such as $P_2S_8^{4-}$, $P_2S_7^{4-}$, or $P_2S_6^{2-}$, and lithium polysulfides Li_2S_n (with $n \geq 1$).[26,27] With regard to the multi-element substituted SEs, the electrochemical decomposition reactions become much more complex, also involving semimetal sulfide species.[16] The results indicate that multi-cation substitution on the phosphorus site reduces the onset potential for oxidation

Table 1. Refined lattice parameter of the different SEs and ionic conductivity determined on cold-pressed pellets at room temperature.

Sample	Composition	Lattice parameter a (Å)	Ionic conductivity (mS cm^{-1})
Equimolar	$Li_{6.5}[P_{0.25}Si_{0.25}Ge_{0.25}Sb_{0.25}]S_5I$	10.29224(12)	12.3
Si-rich	$Li_{6.67}[P_{0.16}Si_{0.5}Ge_{0.16}Sb_{0.16}]S_5I$	10.28330(9)	12.3
Ge-rich	$Li_{6.67}[P_{0.16}Si_{0.16}Ge_{0.5}Sb_{0.16}]S_5I$	10.32186(13)	14.6
I-free	$Li_{5.5}PS_{4.5}Cl_{0.8}Br_{0.7}$	9.89601(29)	8.8
LPSCl*	Li_6PS_5Cl	9.85485(7)	3.4

*From ref. [22] for lattice parameter and from ref. [9] for ionic conductivity.

Batteries & Supercaps

Research Article
doi.org/10.1002/batt.202400112

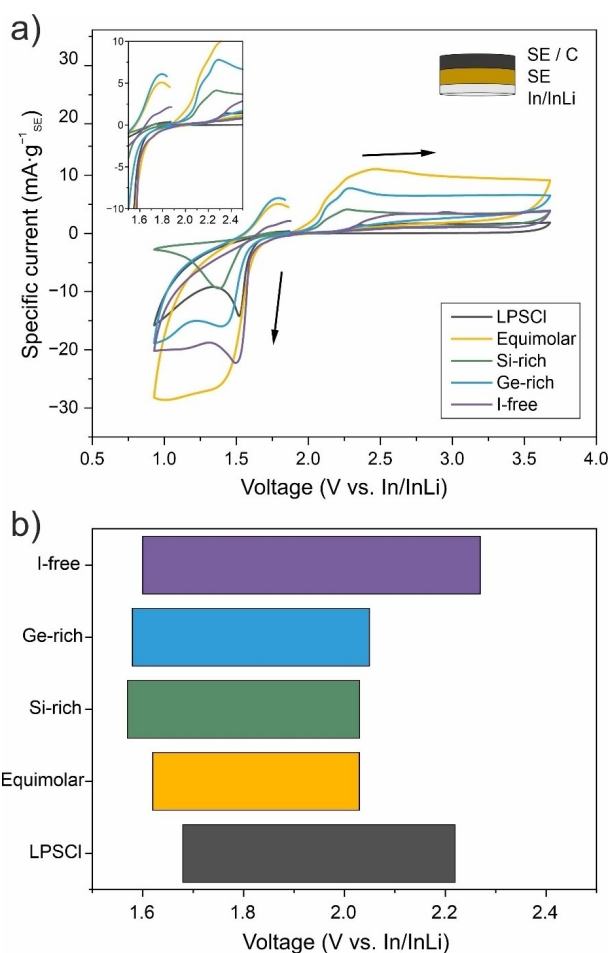**Chemistry Europe**
European Chemical
Societies Publishing

Figure 2. (a) First-cycle CV curves for the different SEs measured at 0.1 mV s^{-1} and 45 °C. The cell configuration used is schematically shown in the inset. (b) The ESWs extracted from the cyclic voltammograms.

by about 250 mV. This implies a lower oxidative stability compared to both the I-free SE and LPSCl, which can be attributed to the lower ionization potential and weaker bonding strength of I$^-$ compared to Br$^-$ and Cl$^-$, causing a somewhat poorer stability for the cationic substituted samples.[28] However, previous research on Li$_{6+x}$P$_{1-x}$M$_x$S$_5$I (M=Si^{4+}, Ge^{4+} and $x=0.6$) SEs has shown that the oxidative stability remains virtually unaltered with 60% phosphorus substitution.[29] In contrast, the data presented herein suggest that complex cation substitution has a more profound effect on the stability. However, we cannot rule out that the higher degree of substitution (>75%, see Table 1) is playing a role as well. We hypothesize that the lower oxidative stability of the cationic substituted SEs is closely related to the strength of the M—S bond and the lattice distortion. The former can be simplified expressed as ionic potential φ of M (with φ being the ratio of the electrical charge z to the ionic radius r), with a higher ionic potential indicating a greater bond strength.[30] For phosphorus (4-fold coordination, +5 oxidation state), a higher ionic potential ($\varphi = 29.41$ Å^{-1}) was calculated compared to silicon ($\varphi = 15.38$ Å^{-1}) and germanium ($\varphi = 10.26$ Å^{-1}) (note: an even lower ionic potential can be

expected for Sb^{5+}), which helps explain the improved anodic stability of purely phosphorus-containing SEs.

According to the Bell-Evans-Polanyi (B—E—P) principle, which delineates kinetic-thermodynamic relationships, oxidative stability not only correlates with the thermodynamic driving force for oxidizing materials, but also depends on the kinetics.[31,32] We believe that multi-cation substitution reduces the oxidative stability by enhancing the kinetics of the electrochemically-driven decomposition reactions (lower barrier for ion diffusion in the distorted lattice).[33] Specifically, the weakened bonds and softened lattice resulting from the complex substitution may facilitate cation and anion mobility, which is reflected in narrower ESWs. Therefore, unlike previous conclusions, it seems that phosphorus substitution directly affects the electrochemical stability of lithium thiophosphates.[25] Moreover, the anodic current was larger in the second and third cycles for all samples, indicating continuous SE degradation (electrochemical oxidation) during cycling (see Figure S2a–e, Supporting Information).

With regard to the cathodic stability, current flow in the initial sweep was clearly noticed below 1.8 V (~2.42 V vs. Li$^+$/Li). According to the literature, this can be attributed to phosphorus reduction, as shown in Equation 2 for LPSCl, and/or reduction of polysulfide species formed previously at higher potentials.[26]

$$Li_6PS_5Cl + 8Li^+ + 8e^- \rightarrow LiCl + Li_3P + 5Li_2S \qquad (2)$$

Upon further cycling (see Figure S2a–e, Supporting Information), the absolute cathodic current decreased, except for the Si-rich SE where a slight increase was observed. The asymmetry between the reductive and oxidative currents points towards irreversible side reactions, especially for the equimolar, Ge-rich, I-free, and LPSCl SEs. It should be noted though that unravelling the decomposition reactions occurring during cycling is very challenging, since not only the thermodynamic stability of the SEs (and decomposition products), but also the kinetic stability of the formed interfaces/interphases plays a decisive role.[33] Nevertheless, the ESWs of the different materials studied in the present work were extracted from the first-cycle CV curves. As can be seen from Figure 2b, the cationic substituted samples exhibit narrow ESWs ranging from around 1.6 to 2.0 V (~2.22–2.62 V vs. Li$^+$/Li). For the other SEs, the window is wider, in particular with respect to oxidative stability, where the upper limit is pushed up to 2.27 V (~2.89 V vs. Li$^+$/Li). Overall, we conclude from the data that altering the composition of thiophosphate SEs affects their anodic and cathodic stability. The ESW decreased in the following order: I-free > LPSCl > Si-rich > Ge-rich > equimolar.

The possibility of using a lithium anode is one of the most promising aspects of SSBs. However, many materials suffer from severe instability when in contact with lithium metal.[34,35] The compatibility of the SEs with lithium was probed at 25 °C using a Li|SE|Li cell configuration. Impedance spectra were recorded directly after assembly and at fixed time intervals up to 24 h without applying external pressure. Figure S3a–e (Supporting Information) shows the respective time-resolved impedance spectra collected from cells containing the different SEs, with all

Batteries & Supercaps

Research Article
doi.org/10.1002/batt.202400112

Chemistry Europe
European Chemical
Societies Publishing

of them revealing the characteristic shape of mixed conducting interfaces/interphases.[36,37] To quantitatively compare the stability among the SEs tested, the spectra were fitted using suitable equivalent circuits, along with distribution of relaxation times (DRT) analysis.[38,39] For the highly conducting, cationic and anionic substituted SEs, the barely visible bulk response at ultrahigh frequencies (7–1 MHz) was described by a simple resistor R. Several RQ elements (Q = constant phase element) were needed to fit the data (depressed semicircles) from the high- to low-frequency range. Their physical meaning was derived from the specific response times (see Figure S4, Supporting Information).[40,41] In Figure 3a–e, the Nyquist plots of the electrochemical impedance recorded after 0 and 24 h are presented together with the fitting results. Summaries of the calculated parameters are given in Tables S4–S8. R_1 and R_2 can be attributed to the bulk SE and the contact resistance between electrode and current collector, respectively. R_3 and R_4 can be

assigned to the interface resistance, comprising various underlying processes, which emphasize the microstructural and chemical complexity of the as-formed interfaces/interphases. For comparison, the total interface resistances (with $R_{total} = R_3 + R_4$) after 0 and 24 h are depicted in Figure 3f. Because of the symmetrical cell configuration, it can be assumed that both sides equally contribute to the total resistance. Therefore, R_{total} was divided by a factor of two to yield resistance values for single Li|SE interfaces. After 24 h, the R_{total} was determined to be 420 Ω for LPSCl, a relatively minor increase compared to the initial value (360 Ω). A clear increase in resistance with time was noticed for the equimolar, Si-rich, and Ge-rich SEs. In these cases, the R_{total} increased from 136 to 372 Ω, 54 to 103 Ω, and 190 to 642 Ω for the equimolar, Si-rich, and Ge-rich SEs, respectively, after 24 h. In contrast, for the I-free SE, a moderate increase in R_{total} by 34 Ω (179 Ω) from the initial value (145 Ω) was observed.
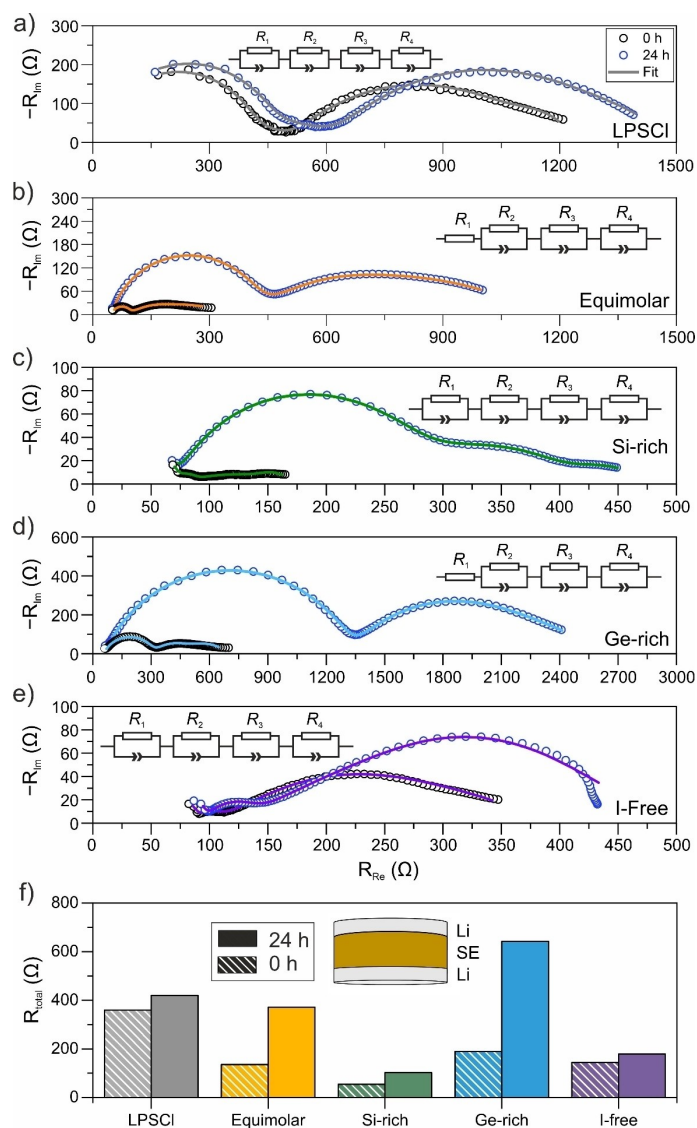

Figure 3. (a–e) Nyquist plots of the electrochemical impedance of symmetrical Li cells using the different SEs after assembly (0 h) and 24 h at 25 °C. Experimental data are shown as empty symbols and curve fits as solid lines. Equivalent circuits used for fitting the data are shown in the insets. (f) Corresponding resistances calculated from the interface and interphase contributions after 0 and 24 h.

Batteries & Supercaps

Research Article
doi.org/10.1002/batt.202400112

Chemistry Europe
European Chemical
Societies Publishing

Taken together, the EIS results point towards decreasing stability against lithium metal upon introducing cationic substituents. Moreover, the data indicate that for the cationic substituted SEs, the as-formed interfaces/interphases are kinetically unstable, leading to continuous degradation and impedance growth. By contrast, both LPSCl and the I-free SE exhibit better stability, with the latter material possessing a relatively low areal interface resistance of 141 Ω cm^2 after 24 h.

Next, the electrochemical performance of the SEs was examined in pelletized SSBs with LiNbO$_3$-coated NCM851005 as cathode active material and an indium-lithium anode. In these experiments, the SEs were contained in the cathode and further served as the separator. The cells were cycled at 45 °C in a potential window of 2.28–3.68 V vs. In/InLi (~2.9–4.3 V vs. Li$^+$/Li) applying current rates ranging from C/2 to 2 C. Figure 4a represents the first- and second-cycle voltage profiles at C/2. The initial specific charge/discharge capacities and the Coulomb efficiencies (CEs) of the first two cycles are plotted in Figure 4b and c, respectively. All cells exhibited initial specific charge capacities exceeding 200 mAh g^{-1}, and they delivered specific discharge capacities of 161 mAh g^{-1} (equimolar), 189 mAh g^{-1} (Si-rich), 191 mAh g^{-1} (Ge-rich), 201 mAh g^{-1} (I-free), and 202 mAh g^{-1} (LPSCl). This translates to CEs of about 79, 79, 84, 89, and 89%, respectively. As evident from these data, employing the cationic substituted SEs leads to poor first-cycle CEs, whereas the reversibility is much improved for LPSCl and the I-free SE. This result confirms that cation substitution negatively affects the electrochemical stability and agrees well with the trend in ESWs determined from the CV experiments (see Figure 2). Nevertheless, the CEs stabilized above 95% from the second cycle onwards.

Subsequently, the rate performance was tested, followed by long-term cycling at C/2. The corresponding specific discharge capacities and CEs are shown in Figure 5a and b, respectively. Upon increasing the C-rate to 2 C, the LPSCl-containing cell was only capable of delivering 120 mAh g^{-1} or less, unlike (especially) the I-fee SE, which allowed for $q_{dis} \geq 160$ mAh g^{-1}. This major difference in rate capability is primarily due to differences in conductivity of the SEs (see Table 1) and the decomposition interphases formed during cycling (leading to impedance buildup). However, the respective cells showed a similar performance during long-term cycling at C/2 and still delivered capacities of ~150 mAh g^{-1} after 75 cycles. In contrast, for the cationic substituted SEs, the capacity fading with cycling at C/2 was much more severe, with $q_{dis} \approx 90$ mAh g^{-1} (equimolar and Ge-rich) and 75 mAh g^{-1} (Si-rich) after 75 cycles. Even though the compositionally complex SEs outperformed the LPSCl at high C-rates for the aforementioned reasons, cells using the cationic substituted materials suffered from severe capacity decay due to their lower electrochemical stability, as outlined above. The stability issues are also apparent from the CEs. In the initial cycles (rate performance testing), the CEs approached or even exceeded 99%. However, only for LPSCl and the I-free SE, they remained on average above 99% during extended
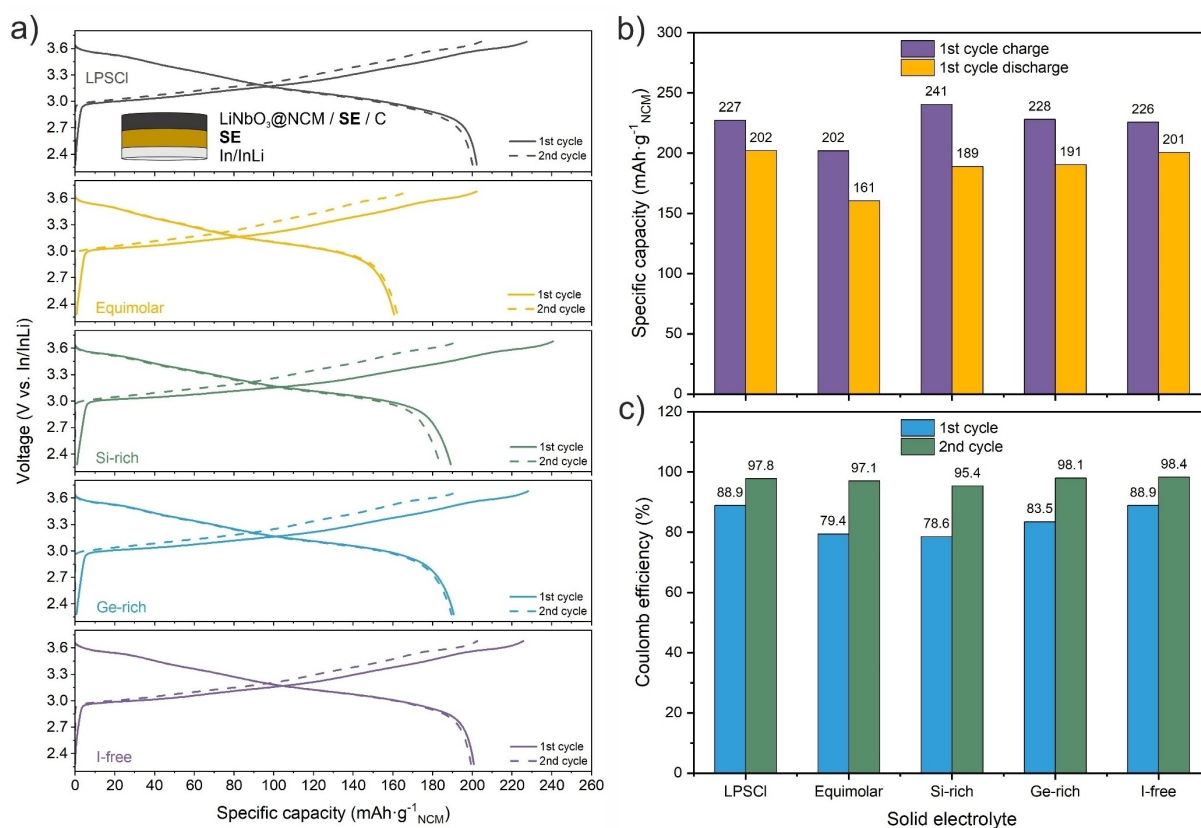

Figure 4. (a) Voltage profiles for the first (solid line) and second (dashed line) cycles of pelletized SSB cells using the different SEs both in the cathode and separator at C/2 rate and 45 °C. (b) Corresponding specific charge/discharge capacities and (c) Coulomb efficiencies.
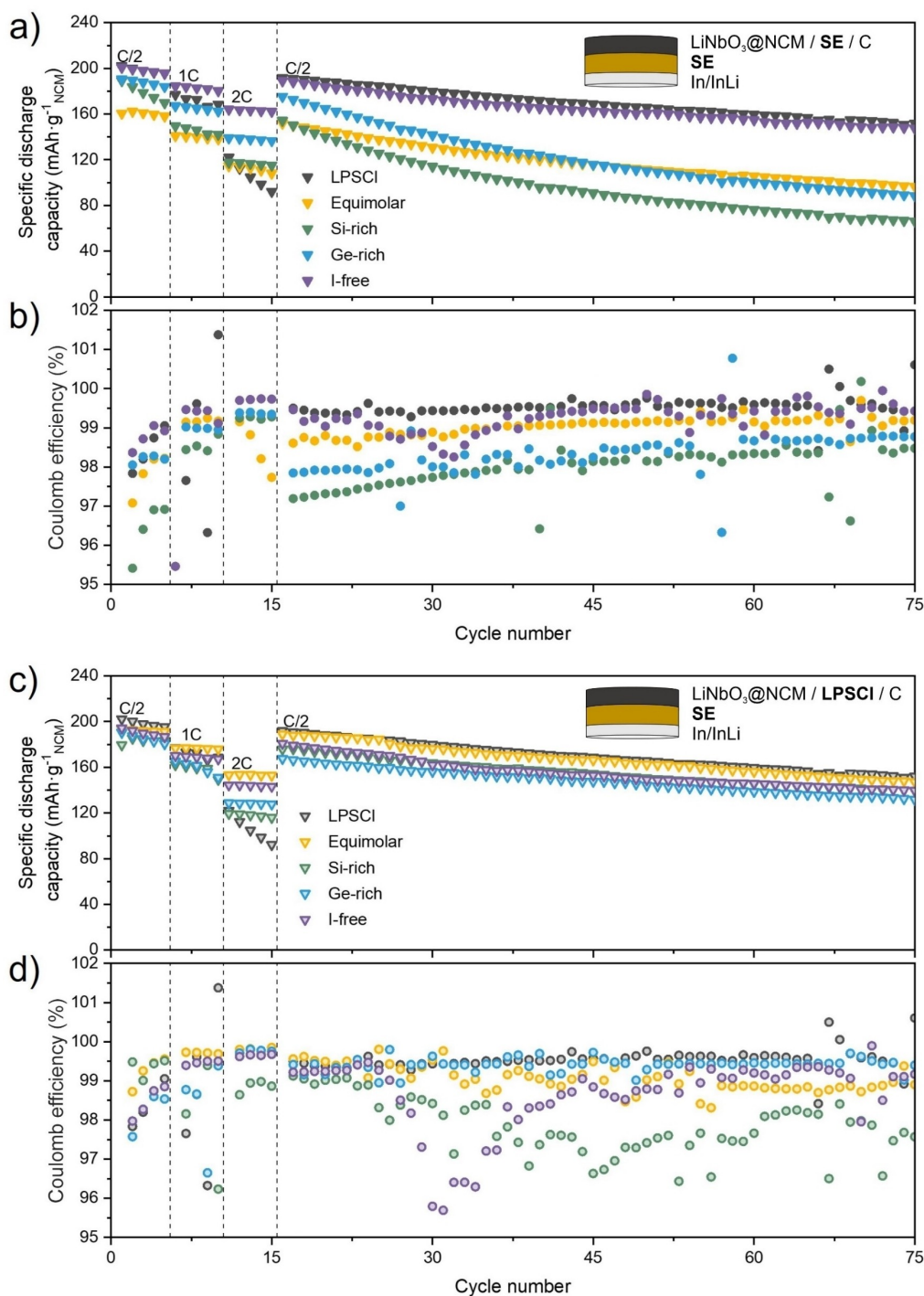
Figure 5. Cycling performance of pelletized SSB cells using the different SEs at 45 °C. (a) Specific discharge capacities at various C-rates and (b) corresponding Coulomb efficiencies. In this configuration [see inset in (a)], the respective SEs were contained in the cathode and served as the separator. (c) Specific discharge capacities at various C-rates and (d) corresponding Coulomb efficiencies achieved with cells using LPSCl in the cathode and the different SEs as the separator [see inset in (c)].

cycling at C/2 rate, corroborating their superiority. It is noteworthy that the trend in electrochemical stability determined from the CV experiments does not directly correlate with the cell cyclability. In fact, it seems that the stability of the decomposition interphases plays an important role too. If the decomposition products formed in the initial cycle(s) are kinetically and/or thermodynamically stable, they would prevent further SE degradation, thus helping to stabilize the cell performance.[42] Yet, the results indicate that the cationic substituted lithium argyrodites in particular do not form stable cathode interfaces and interphases.

Batteries & Supercaps

Research Article
doi.org/10.1002/batt.202400112

Chemistry
Europe

European Chemical
Societies Publishing

To improve the cycling performance, the ion conductor in the cathode was replaced with LPSCl, and the different SEs were only employed as the separator. As can be seen from Figure 2, LPSCl apparently exhibits the best anodic stability among the materials investigated. Therefore, the degradation related to (irreversible) oxidative SE decomposition should be minimized. The cells were subjected to a similar cycling protocol as described above. At first glance, this strategy appears to be successful, as the specific discharge capacities and the fading behavior were similar for the different cells (see Figure 5c). However, on closer examination, it is found that the cell using LPSCl as SE in the cathode and separator again delivered the lowest capacities at 2 C. This is clearly due to the material's ionic conductivity being lower by a factor of three or more compared to the other SEs. The reduced degradation at the positive electrode side when using LPSCl in the cathode is also evident from the CEs (see Figure 5d). Except for the cell using the Si-rich SE, the CEs stabilized above 98% during cycling at C/2. The fact that the Si-rich SE led to poor reversibility in this SSB configuration points towards continuous side reactions (interphase formation) at the In/InLi | SE interface.

After having tested the SEs in two different SSB configurations at 45 °C, similar electrochemical measurements were conducted at 25 °C. The specific discharge capacities of cells where (i) the respective SEs were contained in the cathode and served as separator at the same time and (ii) LPSCl was employed in the cathode and the different SEs only served as separator are presented in Figure 6a and b, respectively. Because the same cycling protocol was applied to the cells, the capacities were somewhat lower at 25 °C, as expected. At a rate of 2 C, LPSCl was outperformed by all other SEs. Also, if the cationic substituted SEs were employed both in the cathode and separator, the overall degradation was much lower (see Figure 6a) compared to that at 45 °C (see Figure 5a). This is indicative of kinetic instabilities. In addition, it is evident from the data in Figure 6b that the ionic resistance of the separator layer has a profound effect on the cycling performance, which is mitigated to some degree at elevated temperatures.

For better comparison of the specific discharge capacities at the different C-rates and temperatures, they are plotted for the cells where the SEs were contained in the cathode and served as separator in Figure 7a and b. As shown in Figure 7a, the cells using the compositionally complex lithium argyrodites delivered similar capacities at 25 °C, ranging from about 100 mAh g^{-1} at 2 C to 170 mAh g^{-1} at C/2. In contrast, the LPSCl-containing cell showed much lower capacities, with only ~50 and 145 mAh g^{-1} at 2 C and C/2, respectively. However, significant differences were observed for the cells cycled at 45 °C (see Figure 7b). The lowest and highest capacities were found for the equimolar and I-free SEs, with differences of more than 40 mAh g^{-1}, virtually independent of the C-rate. The LPSCl-containing cell revealed the strongest increase in q_{dis}, from ~120 mAh g^{-1} at 2 C to 200 mAh g^{-1} at C/2, among the SEs studied here. This finding can be explained by the higher cell resistance resulting from the lower ionic conductivity of LPSCl compared to the cationic and anionic substituted SEs. In addition to the bulk conductivity, the properties of the interfaces and interphases also play a pivotal role in determining the cell performance. Future studies will be dedicated to better understanding ion and electron transport across the interfaces and its effect on cyclability.

3. Conclusions

In summary, we have investigated the electrochemical stability and performance of a series of novel compositionally complex lithium argyrodite solid electrolytes in bulk-type solid-state batteries and benchmarked them against commercially available Li$_6$PS$_5$Cl. The samples tested include cationic and anionic substituted materials, all exhibiting high room-temperature ionic conductivities of $\sigma_{ion} \geq 9$ mS cm^{-1}. Their stability was examined by cyclic voltammetry conducted on carbon-based composite electrodes and by time-resolved electrochemical impedance spectroscopy measurements using symmetrical Li cells. In general, it is found that cation substitution narrows the
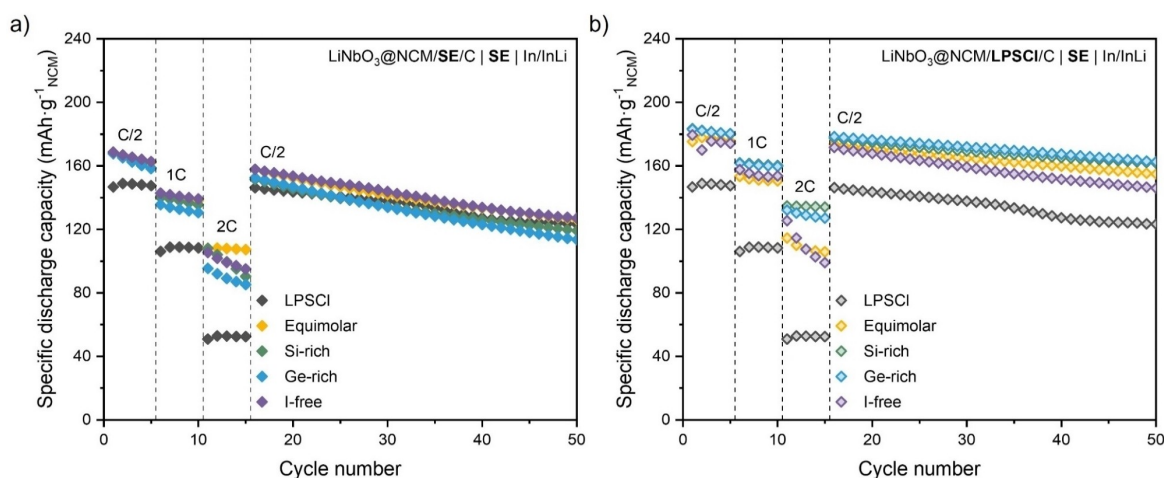

Figure 6. Cycling performance of pelletized SSB cells using the different SEs at 25 °C. (a) The respective SEs were contained in the cathode and served as the separator and (b) LPSCl was employed in the cathode and the different SEs only served as the separator.
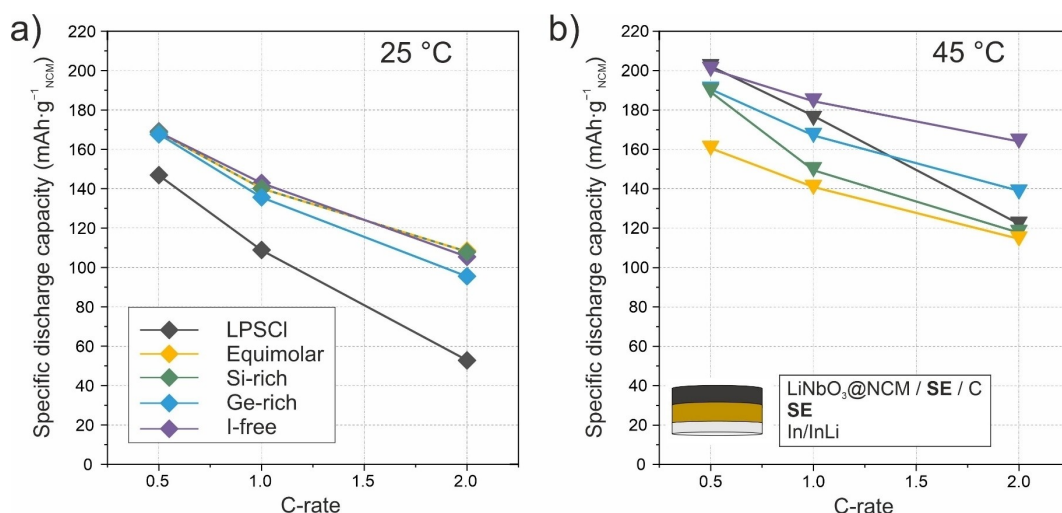
Batteries & Supercaps

Research Article
doi.org/10.1002/batt.202400112

Chemistry Europe
European Chemical
Societies Publishing

Figure 7. Comparison of specific discharge capacities of pelletized SSB cells using the different SEs (a) at 25 °C and (b) at 45 °C. Data taken from the first cycle of each C-rate. The respective SEs were contained in the cathode and served as the separator.

electrochemical stability window of lithium argyrodite solid electrolytes. To evaluate the ion conductors under realistic (practical) conditions, solid-state battery cells were assembled using a surface-protected, Ni-rich $LiNi_xCo_yMn_zO_2$ (NCM or NMC) as cathode active material. At room temperature and high current rates, the compositionally complex solid electrolytes readily outperform the reference Li_6PS_5Cl. However, the lower stability of the cationic substituted materials leads to accelerated capacity fading upon cycling at elevated temperature. Nevertheless, utilizing these materials only in the separator layer positively affects the cell cyclability. In contrast, the anionic substituted solid electrolyte $Li_{5.5}PS_{4.5}Cl_{0.8}Br_{0.7}$ provides low-resistive interfaces with anode and cathode, leading to the overall best performance, specifically at high current rates. This corroborates recent findings that the I-free, high-entropy solid electrolyte enables stable long-term cycling of all-solid-state batteries.[18] Taken together, we have demonstrated that ionic conductivity is not the only important attribute of inorganic solid electrolytes, and that anion prevails over cation substitution in developing advanced materials for solid-state battery application. We believe that the design parameters described in this work provide a blueprint for future solid electrolytes, with multicomponent materials providing virtually unlimited possibilities.

Experimental Section

Materials Synthesis

Unless specified otherwise, the work was performed under inert argon atmosphere in a glovebox (MBraun, with $[O_2]$ and $[H_2O] <$ 0.1 ppm) or using Schlenk line techniques. All chemicals were used as received, and LPSCl was purchased from NEI Corp. In general, stoichiometric mixtures of Li_2S (99.99%, Sigma-Aldrich), P_2S_5 (99%, Sigma-Aldrich), GeS_2 (99.9%, Goodfellow), SiS_2 (99.99%, Goodfellow), Sb_2S_3 (99.99%, Alfa Aesar), and LiI (99.999%, Sigma-Aldrich) plus 10 wt% excess sulfur (99.99%, Sigma-Aldrich) were loaded

into 250 mL zirconia milling jars with 150 g zirconia balls (10 mm diameter). Ampules were pre-dried under dynamic vacuum using a heat gun.

Equimolar ($Li_{6.5}[P_{0.25}Si_{0.25}Ge_{0.25}Sb_{0.25}]S_5I$)

The precursor mixture was milled at 250 rpm for 1 h and then at 450 rpm for 15 h. The recovered powder (~1.2 g) was pelletized at 3 t and vacuum-sealed (10^{-3} bar) in a quartz ampule, followed by annealing at 500 °C for 10 h with heating and cooling rates set to 5 °C min^{-1}.

Si-rich ($Li_{6.67}[P_{0.16}Si_{0.5}Ge_{0.16}Sb_{0.16}]S_5I$) and Ge-rich ($Li_{6.67}[P_{0.16}Si_{0.16}Ge_{0.5}Sb_{0.16}]S_5I$)

The precursor mixture was milled at 250 rpm for 1 h and then at 450 rpm for 40 h, including 10 min rest steps after each 15 min of milling. The recovered powder (~1.2 g) was pelletized at 3 t and vacuum-sealed (10^{-3} bar) in a quartz ampule, followed by annealing at 500 °C for 10 h with heating and cooling rates set to 0.165 and 5 °C min^{-1}, respectively.

I-Free ($Li_{5.5}PS_{4.5}Cl_{0.8}Br_{0.7}$)

The precursor mixture was milled at 250 rpm for 1 h and then at 450 rpm for 15 h. The recovered powder (~1.2 g) was pelletized at 3 t and vacuum-sealed (10^{-3} bar) in a quartz ampule, followed by annealing at 440 °C for 10 h with heating and cooling rates set to 1.5 °C min^{-1}.

Surface Coating of NCM851005 ($LiNi_{0.85}Co_{0.10}Mn_{0.05}O_2$)

The NCM851005 (BASF SE) was first heated for 3 h at 750 °C in oxygen flow of 30 L h^{-1} with heating and cooling rates set to 5 °C min^{-1} to remove surface impurities. To produce a 1.0 wt% $LiNbO_3$ protective coating on the surface of the secondary particles, 410 µL of lithium ethoxide (1.0 M) and 820 µL of niobium ethoxide (0.5 M) in absolute ethanol were added to 5.94 g of NCM851005. The suspension was sonicated for 30 min and then dried in a vacuum overnight. The recovered powder was ground using a mortar and pestle and heated in oxygen for 2 h at 350 °C.[43] XRD

Batteries & Supercaps

Research Article
doi.org/10.1002/batt.202400112

Chemistry Europe
European Chemical
Societies Publishing

patterns and ATR-IR spectra collected before and after coating are presented in Figure S5 (Supporting Information).

Characterization

Laboratory X-ray Diffraction (XRD)

The samples were flame-sealed in borosilicate capillaries (0.68 mm inner diameter, 0.01 mm wall thickness; Hilgenberg) and subjected to XRD using a Stadi-P diffractometer (STOE) with Mo anode ($\lambda = 0.70926$ Å) and a MYTHEN 1 K strip detector (DECTRIS). Rietveld and Le Bail analysis of diffraction data was done with the help of FullProf Suite.[44] The Thompson-Cox-Hastings pseudo-Voigt function was used to describe the peak shape after point-by-point background subtraction. Scale factor, peak shape parameters, lattice parameters, and atomic displacement parameters were refined. The zero-shift parameter was treated last.

Attenuated Total Reflection-Infrared (ATR-IR) Spectroscopy

ATR-IR spectroscopy measurements were performed on an ALPHA FT-IR spectrometer (Bruker). All spectra were background corrected using the OPUS software.

Cyclic Voltammetry (CV)

Solid electrolyte and Super C65 carbon black (TIMCAL) were mixed in a 7:3 weight ratio using a planetary mill (Fritsch) at 140 rpm for 30 min using 70 mL zirconia milling jars with 10 zirconia balls (10 mm diameter) and used as working electrode. The carbon black was dried at 300 °C under dynamic vacuum overnight prior to use. The cells were assembled using a customized setup comprising a PEEK sleeve (10 mm diameter) and two stainless steel dies. 100 mg of solid electrolyte was first compressed at 62 MPa to produce the separator. Around 12 mg of working electrode was then evenly distributed on one side of the separator. The stack was compressed at 437 MPa. Finally, an indium foil (9 mm diameter, 125 μm thickness; Thermo Fisher Scientific) and a lithium foil (6 mm diameter, 50 μm thickness; Albemarle Corp.) were freshly punched out and placed on the other side of the separator, with the indium foil facing the solid electrolyte. CV experiments were performed under an external pressure of 81 MPa between 0.93 and 3.68 V vs. In/InLi (~1.55–4.3 V vs. Li$^+$/Li) at a sweep rate of 0.1 mV s^{-1} and at 45 °C after a resting period at OCV for 30 min using an SP-200 potentiostat (BioLogic). The onset potentials for oxidation and reduction were determined as exemplarily shown for LPSCl in Figure S6 (Supporting Information).

Time-Resolved Electrochemical Impedance Spectroscopy (EIS)

EIS measurements were conducted on symmetrical cells (Li|SE|Li) at 25 °C without additional external pressure. To this end, about 150 mg of solid electrolyte was compressed at 437 MPa. Lithium foils (6 mm diameter, 50 μm thickness) were freshly punched out and placed at both sides of the separator. Impedance data were collected using a VMP-3 potentiostat (BioLogic) over a frequency range from 7 MHz to 100 mHz with an AC voltage amplitude of 20 mV. The first spectrum was measured immediately after cell assembly (0 h). Subsequent spectra were recorded after 2, 4, 6, 10, 16, and 24 h. Evaluation of the EIS data and DRT analysis were performed using the software RelaxIS 3.0.22 (rhd instruments).

Galvanostatic Cycling

For battery performance tests, cathode composites were prepared by mixing the LiNbO$_3$-coated NCM851005, solid electrolyte, and Super C65 in a 69.3:29.7:1 weight ratio using a planetary mill at 140 rpm for 30 min with 70 mL zirconia milling jars containing 10 zirconia balls (10 mm diameter). Cells were assembled in similar manner as described above for the CV testing. The loading was ~10.5 mg$_{NCM}$ cm^{-2}. Galvanostatic cycling was performed at 45 °C and under an external pressure of 81 MPa in a potential window of 2.28–3.68 V vs. In/InLi (~2.9–4.3 V vs. Li$^+$/Li) after resting at OCV for 1 h using a MACCOR battery cycler. The C-rate was varied from C/2 to 2 C, with 1 C = 190 mA g$_{NCM}^{-1}$.

Supporting Information

Supporting Information is available from the Wiley Online Library or from the author.

Conflict of Interests

A patent was filed for some of this work through BASF SE and the Karlsruher Institut für Technologie (KIT).

Data Availability Statement

The data that support the findings of this study are available from the corresponding author upon reasonable request.

[1] A. L. Robinson, J. Janek, *MRS Bull.* **2014**, *39*, 1046–1047.
[2] J. Janek, W. G. Zeier, *Nat. Energy* **2023**, *8*, 230–240.
[3] P. Minnmann, L. Quillman, S. Burkhardt, F. H. Richter, J. Janek, *J. Electrochem. Soc.* **2021**, *168*, 40537.
[4] Y. Kato, S. Shiotani, K. Morita, K. Suzuki, M. Hirayama, R. Kanno, *J. Phys. Chem. Lett.* **2018**, *9*, 607–613.
[5] Z. Zhang, Y. Shao, B. Lotsch, Y. S. Hu, H. Li, J. Janek, L. F. Nazar, C. W. Nan, J. Maier, M. Armand, L. Chen, *Energy Environ. Sci.* **2018**, *11*, 1945–1976.

[6] P. Minnmann, F. Strauss, A. Bielefeld, R. Ruess, P. Adelhelm, S. Burkhardt, S. L. Dreyer, E. Trevisanello, H. Ehrenberg, T. Brezesinski, F. H. Richter, J. Janek, *Adv. Energy Mater.* **2022**, *12*, 2201425.

[7] H.-J. Deiseroth, S.-T. Kong, H. Eckert, J. Vannahme, C. Reiner, T. Zaiß, M. Schlosser, *Angew. Chem. Int. Ed.* **2008**, *47*, 755–758.

[8] H.-J. Deiseroth, J. Maier, K. Weichert, V. Nickel, S.-T. Kong, C. Reiner, *Z. Anorg. Allg. Chem.* **2011**, *637*, 1287–1294.

[9] R. Schlenker, A.-L. Hansen, A. Senyshyn, T. Zinkevich, M. Knapp, T. Hupfer, H. Ehrenberg, S. Indris, *Chem. Mater.* **2020**, *32*, 8420–8430.

[10] A. Gautam, M. Sadowski, M. Ghidiu, N. Minafra, A. Senyshyn, K. Albe, W. G. Zeier, *Adv. Energy Mater.* **2021**, *11*, 2003369.

[11] J. Lau, R. H. DeBlock, D. M. Butts, D. S. Ashby, C. S. Choi, B. S. Dunn, *Adv. Energy Mater.* **2018**, *8*, 1800933.

[12] J. H. Teo, F. Strauss, F. Walther, Y. Ma, S. Payandeh, T. Scherer, M. Bianchini, J. Janek, T. Brezesinski, *Mater. Futures* **2022**, *1*, 015102.

[13] M. A. Kraft, S. Ohno, T. Zinkevich, R. Koerver, S. P. Culver, T. Fuchs, A. Senyshyn, S. Indris, B. J. Morgan, W. G. Zeier, *J. Am. Chem. Soc.* **2018**, *140*, 16330–16339.

[14] L. Zhou, A. Assoud, Q. Zhang, X. Wu, L. F. Nazar, *J. Am. Chem. Soc.* **2019**, *141*, 19002–19013.

[15] F. Strauss, J. Lin, M. Duffiet, K. Wang, T. Zinkevich, A.-L. Hansen, S. Indris, T. Brezesinski, *ACS Materials Lett.* **2022**, *4*, 418–423.

[16] J. Lin, G. Cherkashinin, M. Schäfer, G. Melinte, S. Indris, A. Kondrakov, J. Janek, T. Brezesinski, F. Strauss, *ACS Materials Lett.* **2022**, *4*, 2187–2194.

[17] P. Adeli, J. D. Bazak, K. H. Park, I. Kochetkov, A. Huq, G. R. Goward, L. F. Nazar, *Angew. Chem. Int. Ed.* **2019**, *58*, 8681–8686.

[18] S. Li, J. Lin, M. Schaller, S. Indris, X. Zhang, T. Brezesinski, C.-W. Nan, S. Wang, F. Strauss, *Angew. Chem. Int. Ed.* **2023**, *62*, e202314155.

[19] S. V. Patel, S. Banerjee, H. Liu, P. Wang, P.-H. Chien, X. Feng, J. Liu, S. P. Ong, Y.-Y. Hu, *Chem. Mater.* **2021**, *33*, 1435–1443.

[20] J. Lin, M. Schaller, G. Cherkashinin, S. Indris, J. Du, C. Ritter, A. Kondrakov, J. Janek, T. Brezesinski, F. Strauss, *Small* **2024**, *20*, 2306832.

[21] R. D. Shannon, *Acta Crystallogr.* **1976**, *32*, 751–767.

[22] G. F. Dewald, S. Ohno, M. A. Kraft, R. Koerver, P. Till, N. M. Vargas-Barbosa, J. Janek, W. G. Zeier, *Chem. Mater.* **2019**, *31*, 8328–8337.

[23] F. Han, Y. Zhu, X. He, Y. Mo, C. Wang, *Adv. Energy Mater.* **2016**, *6*, 1501590.

[24] D. H. S. Tan, E. A. Wu, H. Nguyen, Z. Chen, M. A. T. Marple, J.-M. Doux, X. Wang, H. Yang, A. Banerjee, Y. S. Meng, *ACS Energy Lett.* **2019**, *4*, 2418–2427.

[25] J. Auvergniot, A. Cassel, D. Foix, V. Viallet, V. Seznec, R. Dedryvère, *Solid State Ionics* **2017**, *300*, 78–85.

[26] R. Koerver, F. Walther, I. Aygün, J. Sann, C. Dietrich, W. G. Zeier, J. Janek, *J. Mater. Chem. A* **2017**, *5*, 22750–22760.

[27] S. Wang, M. Tang, Q. Zhang, B. Li, S. Ohno, F. Walther, R. Pan, X. Xu, C. Xin, W. Zhang, L. Li, Y. Shen, F. H. Richter, J. Janek, C.-W. Nan, *Adv. Energy Mater.* **2021**, *11*, 2101370.

[28] T. Famprikis, P. Canepa, J. A. Dawson, M. S. Islam, C. Masquelier, *Nat. Mater.* **2019**, *18*, 1278–1291.

[29] A. Banik, Y. Liu, S. Ohno, Y. Rudel, A. Jiménez-Solano, A. Gloskovskii, N. M. Vargas-Barbosa, Y. Mo, W. G. Zeier, *ACS Appl. Energ. Mater.* **2022**, *5*, 2045–2053.

[30] G. H. Cartledge, *J. Am. Chem. Soc.* **1928**, *50*, 2855–2863.

[31] M. G. Evans, M. Polanyi, *Trans. Faraday Soc.* **1938**, *34*, 11–24.

[32] S. Muy, J. C. Bachman, L. Giordano, H.-H. Chang, D. L. Abernathy, D. Bansal, O. Delaire, S. Hori, R. Kanno, F. Maglia, S. Lupart, P. Lamp, Y. Shao-Horn, *Energy Environ. Sci.* **2018**, *11*, 850–859.

[33] S. Schweidler, M. Botros, F. Strauss, Q. Wang, Y. Ma, L. Velasco, G. C. Marques, A. Sarkar, C. Kübel, H. Hahn, J. Aghassi-Hagmann, T. Brezesinski, B. Breitung, *Nat. Rev. Mater.* **2024**, *9*, 266–281.

[34] T. Krauskopf, F. H. Richter, W. G. Zeier, J. Janek, *Chem. Rev.* **2020**, *120*, 7745–7794.

[35] J. Janek, W. G. Zeier, *Nat. Energy* **2016**, *1*, 16141.

[36] P. Bron, B. Roling, S. Dehnen, *J. Power Sources* **2017**, *352*, 127–134.

[37] L. M. Riegger, R. Schlem, J. Sann, W. G. Zeier, J. Janek, *Angew. Chem. Int. Ed.* **2021**, *60*, 6718–6723.

[38] H. Sumi, H. Shimada, Y. Yamaguchi, T. Yamaguchi, Y. Fujishiro, *Electrochim. Acta* **2020**, *339*, 135913.

[39] N. Tanibata, S. Takimoto, K. Nakano, H. Takeda, M. Nakayama, H. Sumi, *ACS Materials Lett.* **2020**, *2*, 880–886.

[40] Y. Lu, C.-Z. Zhao, J.-Q. Huang, Q. Zhang, *Joule* **2022**, *6*, 1172–1198.

[41] P. S. Sabet, G. Stahl, D. U. Sauer, *J. Power Sources* **2020**, *472*, 228189.

[42] A. Banerjee, X. Wang, C. Fang, E. A. Wu, Y. S. Meng, *Chem. Rev.* **2020**, *120*, 6878–6933.

[43] S. Payandeh, F. Strauss, A. Mazilkin, A. Kondrakov, T. Brezesinski, *Nano Res. Energy* **2022**, *1*, 9120016.

[44] J. Rodríguez-Carvajal, *Phys. B* **1993**, *192*, 55–69.